Structural, dielectric, impedance, and electric modulus properties of Cu^{2+}-substituted $Cu_xMn_{1-x}Fe_2O_4$ spinel ferrites nanoparticles

Naimatullah Channa[1], Muhammad Khalid[2,*], Ali Dad Chandio[3], Muhammad Saeed Akhtar[4,*] (iD),
Junaid Kareem Khan[5], Ghulam Mustafa[5], Muniba[5], and Zaheer Abbas Gilani[2]

[1] *Department of Physics, Shah Abdul Latif University, Khairpur 66111, Pakistan*

[2] *Department of Physics, Engineering and Management Sciences, Balochistan University of Information Technology, Quetta 87300, Pakistan*

[3] *Department of Metallurgical Engineering, NED University of Engineering and Technology, Karachi 75270, Pakistan*

[4] *Department of Physics, University of Education, Lahore, Pakistan*

[5] *Department of Physics, NED University of Engineering and Technology, Karachi 75270, Pakistan*

ABSTRACT

Copper-substituted manganese ($Mn_{1-x}Cu_xFe_2O_4$) spinel ferrite nanoparticles have been synthesized by adopting sol–gel self-combustion chemical route where $0.0 \leq x \leq 0.5$. All samples were sintered at temperature of 600 °C for three hours to achieve stable crystalline structure of ferrites. XRD analysis revealed that ferrite nanoparticles exhibit face-centered cubic (FCC) structure. The $Mn_{1-x}Cu_xFe_2O_4$ spinel ferrite nanoparticles have been grown with preferred orientation along (311) plane. The crystallite size was estimated through Scherrer's equation and observed to be 17–18 nm. The impedance spectroscopy was employed to investigate the electrical and dielectric characteristics of synthesized samples. The tangent loss was observed to decrease with copper (Cu^{2+}) concentration. The effect of tangent loss, dielectric constant, imaginary dielectric constant, real impedance, imaginary impedance loss, modulus, real and imaginary modulus have been studied in the applied electric field frequency ranging from 20 Hz to 20 MHz for all the samples. The real part of impedance was observed to decrease as a function of Cu^{2+} concentration and frequency, suggesting the decrement in conductivity of the samples. The prepared $Mn_{1-x}Cu_xFe_2O_4$ spinel ferrite nanoparticles would have potential viability in microwave applications.

Address correspondence to E-mail: khalid.mesp@gmail.com; saeed.akhtar@ue.edu.pk

1 Introduction

Last decade and so, the nanomaterials make our life easier, comfortable, and well-appointed due to their high surface to volume ratio. They are extensively used in different fields such as bio-sensing, storage devices, and chromatic imaging. [1, 2]. Recently, the researchers are interested in spinel ferrites especially metal-substituted manganese ferrites since they exhibit novel properties and would have potential use in various fields such as electronics, ferrofluids, and magnetic storage technology [3]. In addition, these materials have applications in dispersion and storage of energy, catalysis, biotechnology, gas sensing, and particularly in carrier fluid due to surface dispersion [4–6]. Owing to compositional, morphological, and topographical behaviors, these materials are being widely used in biomedicine [7]. Firstly, their quantum size is comparable to those of cells ranging from 10 to 100 nm, proteins ranging from 5 to 50 nm, viruses ranging from 20 to 450 nm, or DNA ranging from 10 to 100 nm in length and 2 nm in width. Secondly, these spinel ferrites have intrinsic ability to penetrate in human body due to their magnetic anisotropy. Thirdly, spinel ferrite NPs can be designed to perform specific functionalities [8]. Therefore, NPs have been used as catalyst in magnetic resonance imaging (MRI) or as delivery of anticancer drug or gene delivery [9]. The quantum sized particles (< 10 nm) are utilized in angiography and tumor permeability.

In spinel ferrites, AB_2O_4, unit cell has 32 oxygen atoms that are closely packed. There are 64 tetrahedral A sites and 32 octahedral B sites present in a unit cell consisting of 32 oxygen ions [10]. The structure of spinel ferrite is not electrically neutral because + 2 or + 3 valence metals ions occupy all these sites. Due to this reason, positive charge is dominant in the ferrites. Thus, 8 tetrahedral A sites are occupied instead of 64 tetrahedral A sites. Similarly, 16 octahedral B sites occupied instead of 32 octahedral B sites. Manganese spinel ferrite having 8 formula units $MnOFe_2O_3$ and O_{h7} (Fd3m) group space [11] with 227 group number. The spinel ferrite's feature is the face-centered cubic (FCC) phase in which oxygen anions are attempted to adjust their position called oxygen parameter [12, 13]. The physical properties such as magnetic and dielectric properties purely depend upon the cation's distribution, i.e., divalent metal cations. These properties will alter without disturbing the lattice structure since they rely on the precursor metal ions and the dopant material [14].

Seculic and Milutinovic [15] prepared manganese spinel ferrite via soft mechanochemical route and have noticed dielectric characteristics of the manganese spinel ferrite depend on interaction of grains and grain boundaries. Furthermore, the sintered temperature inversely affects the relaxation time. Zakaullah et al. [16] have fabricated ferrites by using sol–gel auto-combustion route and observed the variation in lattice and dielectric parameters as a function of sintering temperature and frequency. Farooq et al. [17] have synthesized manganese ferrites by using coprecipition method and investigated the structural and dielectric properties of these materials. The effect of Mn–Fe ratio, sintered time, and temperature on the dielectric properties of Mn-ferrites have been reported.

At the quantum level, spinel ferrite nanomaterials can control electrical transport properties and can be fabricated *via* various techniques such as sol–gel route [18], solid-state reaction method [19, 20], hydrothermal technique [21], chemical coprecipitation method [22], citrate precursor route [23], combustion method [24], freeze drying technique [25], and reverse micelle method [26]. Among all routes, sol–gel auto-combustion route has been widely used since it is simple, easy, effective, eco-friendly method with low-sintered temperature.
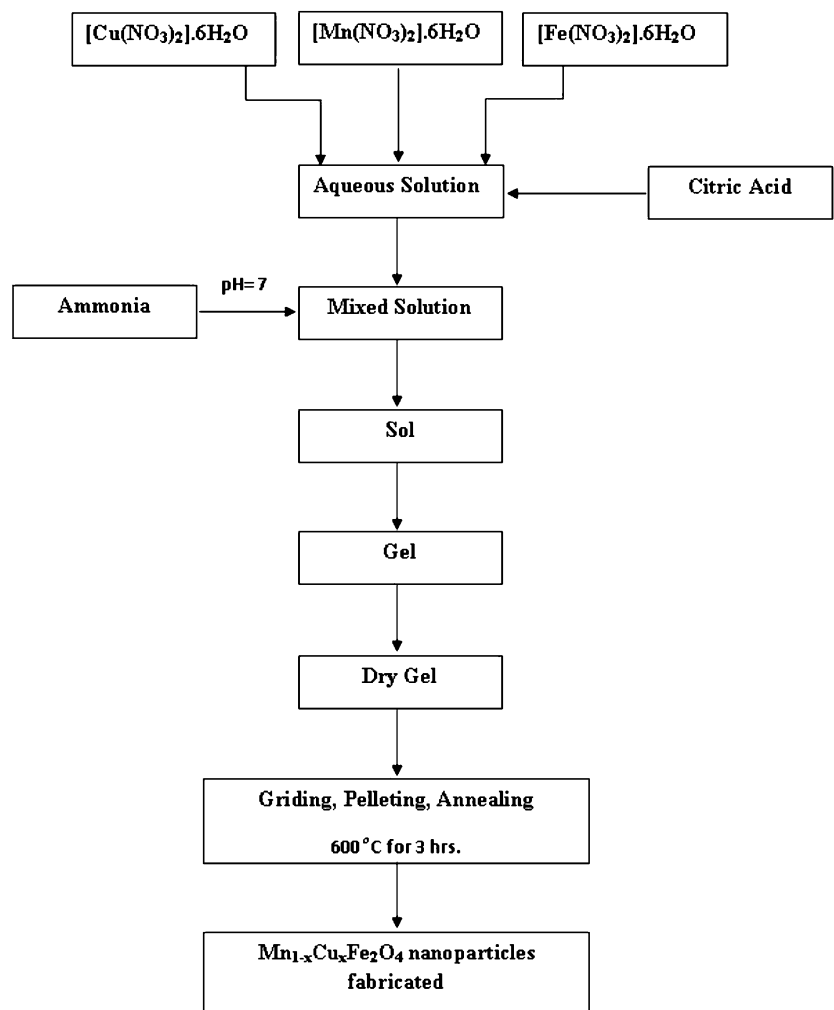
In this research work, the copper-substituted manganese NPs ($Mn_{1-x}Cu_xFe_2O_4$) with $0.0 \leq \times \leq 0.5$ have been synthesized by sol–gel auto-combustion method. The structural, dielectric, and electrical characteristics have been investigated by using X-ray powder diffraction (XRD) method, and impedance analyzer, respectively.

2 Experimental procedure

The copper-substituted manganese ferrites nanoparticles ($Mn_{1-x}Cu_xFe_2O_4$) with $0.0 \leq \times \leq 0.5$ were synthesized through sol–gel auto-combustion method. The precursors, manganese (II) nitrate $[Mn(NO_3)_2].6H_2O$, copper (II) nitrate $[Cu(NO_3)_2].6H_2O$, and iron (III) nitrate $[Fe(NO_3)_2].6H_2O$ purchased from Sigma Aldrich with 98% purity were weighed precisely with digital balance with 0.5, 0.5 and 1 molar ratio and dissolved in de-ionized water separately. Citric acid as fuel mediator with 0.5–1

molar ratio between metal nitrate and citric acid have also been used. The mixed solutions were placed at hotplate with magnetic stirrer under continuous vigorous stirring at temperature 100 °C for 45 min, until it converted into dense solution called sol. The sol was then further transformed into 3D network called gel. After the gel formation, magnetic stirrer was removed and the temperature of the hotplate was enhanced to 250 °C and maintained till the solution burnt due to self-propagating exothermic reaction. The gel became dry amorphous powder, which was further grinded with mortar pestle. The fine powder was sintered at 600 °C for 3 h to achieve required cubic phase. The sintered powder was quenched with hydraulic presser and converted into pellets. These pellets were investigated for structural, electric, and dielectric parameters. The flow chart of synthesis methodology is given in Fig. 1.

The powder X-ray diffraction (XRD) technique was employed to analyze the phase structure of the samples. XRD patterns revealed growth of single-phase crystalline structure of ferrites and α-ferrites. The average size of crystallites was estimated with help of Scherrer's relation for (311) diffraction plane [27]. The electrical and dielectric characteristics of ferrite nanoparticles were analyzed with impedance analyzer; Wayne Kerr 6520P LCR meter, which is an imperative technique to understand the electrical and dielectric behavior of the samples.

3 Results and Discussion

The copper-substituted manganese spinel ferrite nanoparticles were synthesized through sol–gel auto-combustion technique and characterized to study the structural and dielectric properties [28]. The spinel

Fig. 1 Flow chart for sol–gel process of $Mn_{1-x}Cu_xFe_2O_4$ samples

structure of the ferrite was determined through XRD patterns, whereas dielectric properties were extracted from tangent loss and dielectric constant [29]. The properties like crystalline structure, surface layer, crystalline boundaries, and relative dielectric constant are observed to rely on cations distribution.

3.1 Structural analysis

X-ray diffractometer was used to draw powder diffraction patterns of $Mn_{1-x}Cu_xFe_2O_4$ spinel ferrites nanoparticles as shown in Fig. 2. The samples were scanned through 2θ range from 20 to 80° using Cu–Kα radiation source with $\lambda = 1.5405$Å. The observed diffraction peaks correspond to (220), (311), (400), (422), (333), and (440) planes which are well matched with JCPD No. 03-0875 [30]. The XRD data revealed that prepared samples exhibit single-phase crystalline structure with α-ferrite. The most intense diffraction peak corresponding to (311) plane depicted the preferential growth of material along that plane.

The crystallite size was estimated with the help of Scherrer's relation [30].

$$d = \frac{k\lambda}{\beta \cos\theta} \tag{1}$$

Here d represents the particle size, β represents the full width at half maximum, θ represents the diffraction angle, λ represents the wavelength of X-rays, and k is the shape factor whose value is taken as
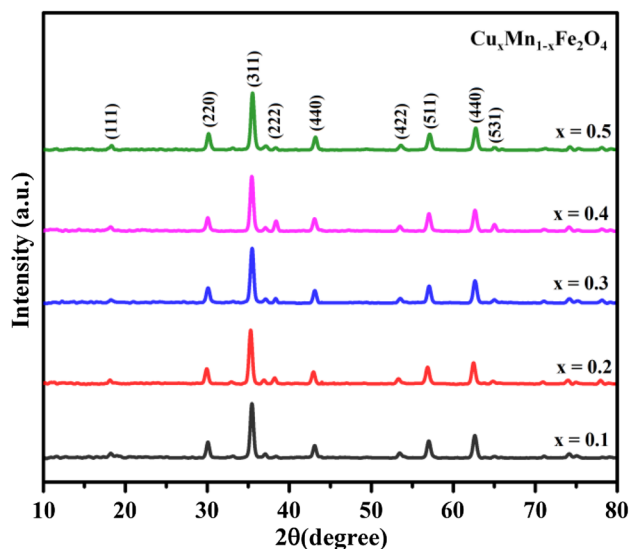

Fig. 2 XRD patterns of prepared $Mn_{1-x}Cu_xFe_2O_4$ samples with $x = 0.1, 0.2, 0.3, 0.4,$ and 0.5

0.89. The average size of the crystallites was observed to be 17.7 nm. However, large crystallite size will decrease the magnetic properties of ferrite materials since it leads to a low signal to noise ratio [31]. The lattice constant was calculated using the following relation [32]:

$$a = d\sqrt{h^2 + k^2 + l^2} \tag{2}$$

Here a represents the lattice parameter and (hkl) represents the Miller indices. The dislocation density was estimated using the following expression:

$$\varepsilon = \frac{\beta}{4\pi \tan\theta} \tag{3}$$

Here ε represents the lattice dislocation, β represents the full width at half maximum, and θ represents the angle of diffraction. The dislocation density of the samples can be extracted using the following expression:

$$\delta = \frac{1}{d^2} \tag{4}$$

Here δ represents the dislocation density and d is crystallite size of ferrite nanoparticles. The structural parameters of the copper-substituted manganese ferrite nanoparticles are listed in Table 1. The variation in lattice constant and crystallite size as a function of copper substitution is shown in Fig. 3.

The microstrain of the ferrite samples was determined by using the following expression:

$$\varepsilon_{micro} = \frac{\beta \cos\theta}{4} \tag{5}$$

Here ε_{micro} represents the microstrain, β represents the full width at half maximum, and θ represents the angle of diffraction. The stacking fault of the ferrite samples was calculated by using following relation:

$$SF = \frac{2\pi^2}{45\sqrt{3}\tan\theta} \tag{6}$$

Here SF is the stacking fault and θ is the diffraction angle.

The X-ray density was calculated by using the relation [33];

$$\rho_x = \frac{8M}{N_A a^3} \tag{7}$$

Here ρ_x represents the X-ray density, M represents the molecular mass, N_A is the Avogadro's number (6.023×10^{23} molecules), and a represents the lattice parameter. The bulk density was calculated as [34];

Table 1 Structural parameters such as lattice parameters, volume density, crystalline size, dislocation density, lattice strain, microstrain and stacking fault, bulk density, X-ray density, surface area of copper-substituted manganese ($Mn_{1-x}Cu_xFe_2O_4$) spinel ferrites nanoparticles

Cu Concentration	d nm	a	$\delta \times 10^{-4}$	$\varepsilon \times 10^{-4}$	$\varepsilon_{micro} \times 10^{-4}$	SF	ρ_x g/cm^3	ρ_m g/cm^3	S cm^2/g
$x = 0.1$	17.72	8.388	31.84	64.23	19.55	0.4480	5.21	2.46	64.98
$x = 0.2$	17.94	8.423	31.05	63.69	19.31	0.4491	5.16	2.47	64.79
$x = 0.3$	17.51	8.384	32.59	64.94	19.78	0.4479	5.25	2.48	65.23
$x = 0.4$	17.80	8.391	31.55	63.95	19.46	0.4481	5.26	2.50	64.06
$x = 0.5$	17.46	8.370	32.79	65.04	19.84	0.4475	5.32	2.505	64.58

Fig. 3 Variation in crystalline size and lattice constant as function of Cu content
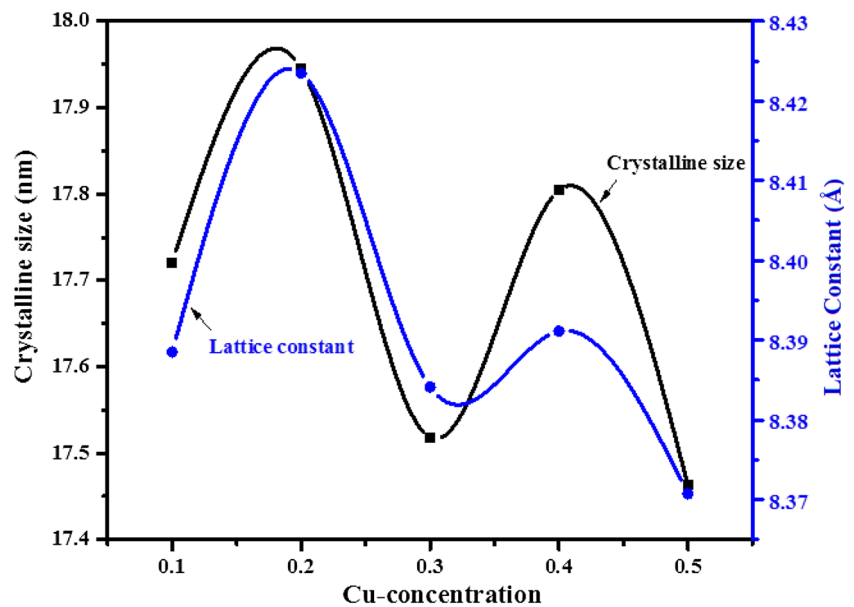
$$\rho_m = \frac{m}{\pi r^2 h} \tag{8}$$

Here ρ_m represents the bulk density, m represents the mass of pellets, r represents the radius of pellets, and h represents the thickness of pellets. The surface area of pellets was determined by using following expression:

$$S = \frac{x}{\rho_x d} \tag{9}$$

Here x is the constant whose value is 6000, ρ_x is the X-ray density, and d is the size of particles. The porosity of the ferrite samples was calculated as follows:

$$P = 1 - \frac{\rho_x}{\rho_m} \tag{10}$$

Here P is the porosity of pellets, ρ_x is the X-ray density, and ρ_m is the bulk density of pellets. The variation in X-ray density and bulk density as function of Cu contents in $Cu_xMn_{1-x}Fe_2O_4$ spinel ferrites is shown in Fig. 4.

3.2 FTIR analysis

FTIR spectra of copper-substituted manganese ferrite samples were recorded in the rage from 400 to 1000 cm^{-1} as depicted in Fig. 5. The spectra reveled the existence of a vibration band at around 550 cm^{-1} due to the stretching vibration at A sites, whereas a
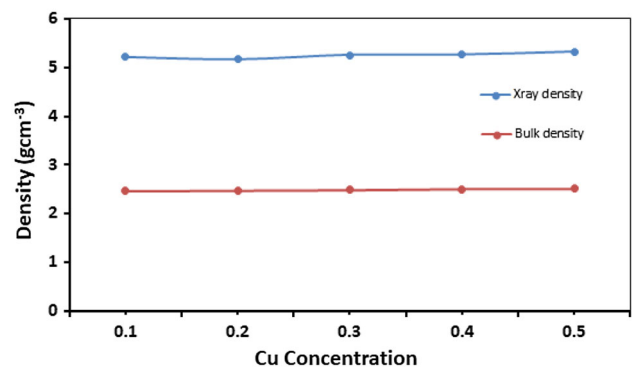
Fig. 4 Variation in X-ray density and bulk density as function of Cu content

vibration band at around 400 cm^{-1} due to stretching vibration at B sites [35]. These frequency bands υ_1 and υ_2 correspond to tetrahedral and octahedral sites as summarized in Table 2. It has been observed that absorption bands significantly shift as a function of Cu^{2+} concentration in the ferrites. The bond length between metal and oxygen ions and change of absorption band frequency that related to the A sites and B sites is linearly influenced by force constant. Furthermore, force constant at tetrahedral sites, F_T and force constant, F_O at octahedral sites were estimated as [36];

$$F = 4\pi^2 c^2 v^2 \mu \tag{11}$$

Here F indicates the force constant, c indicates the speed of light, c = 2.99 × 10^8 ms^{-1}, v indicates the vibration frequency range of tetrahedral and octahedral sites, and μ indicates the reduced mass of Fe^{3+} ions and O^{2-} ions ($\sim$2.065 × 10^{-26} kg mol^{-1}). Force constant for tetrahedral site lies in the range from 2.02 × 10^{-2} to 1.98 × 10^{-2} Nm^{-1}, whereas for octahedral site it is lies at 1.22 × 10^{-2} Nm^{-1}. The substitution of Cu^{2+} affects the force constant as mentioned in Table 2 that resulted from cations redistribution between A sites [37].

3.3 Dielectric properties

The impedance spectroscopy is a suitable technique to investigate the electrical properties and time relaxation characteristics. It can be used to study the
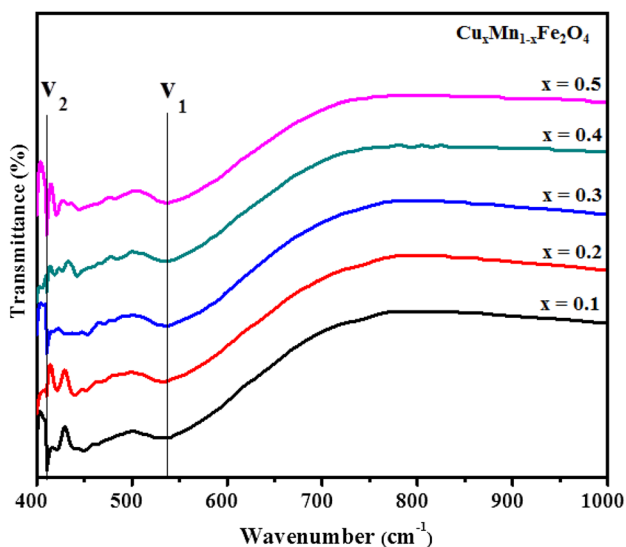

Fig. 5 FTIR spectra of Cu-substituted $Cu_xMn_{1-x}Fe_2O_4$ where x = 0.1, 0.2, 0.3, 0.4, and 0.5

impedance behavior of substance and can analyze the ideal circuit model with discrete electrical component. The effect of dielectric parameters like tangent loss, relative dielectric constant, complex dielectric constant; impedance factors; real and imaginary, modulus; real and imaginary as a function of copper substitution was observed for all the samples in the frequency range from 20 Hz to 20 MHz. Generally, the dielectric properties depend upon the strength of electromagnetic interactions between phases, their structure, and phase dominance. The dielectric loss (tanδ) was determined as a function of frequency by the following relation [38]:

$$\tan\delta = \frac{1}{2\pi f R_p C_p}, \tag{12}$$

where tanδ represents the dielectric loss, f represents frequency of applied electric field, R_p represents the parallel resistance, and C_p represents the capacitance of pellets. The dielectric has important role in the conduction mechanism of any material. The stoichiometric ratios Fe^{2+} ion's variation and feature's homogeneity have been influenced by dielectric loss in ferrites. However, it extensively depends on morphological features and fabrication techniques. Figure 6 shows the strong dispersion in dielectric loss at hoping frequency and synchronization point. This happens due to the conduction phenomenon and dielectric mechanism in the ferrites. The dielectric loss was firstly observed to increase and decreases at low frequency with Cu^{2+} substitution in the ferrites whereas saturated at high frequencies.

The relative dielectric constant was obtained from the following expression:

$$\varepsilon_r = \frac{C_p t}{A \varepsilon_0}, \tag{13}$$

where ε_r is relative dielectric constant of the medium, C_p is parallel capacitance, t is the thickness of pellets, A and ε_o are area and permittivity in free space, respectively. The relative dielectric constant indicated the capacitive behavior of spinel ferrite nanoparticles as shown in Fig. 7. The variations in trend of relative dielectric constant in the copper-substituted manganese ferrite samples were observed due to space charge polarization. According to Maxwell–Wagner two-layer model, space charge polarization induced due to the inhomogeneous morphology of material. For a range of frequency, the dielectric constant initially decreases exponentially at lower frequency and

Table 2 FTIR absorption band and force constant of octahedral and tetrahedral sites

Parameters	v_1 (cm^{-1})	v_2 (cm^{-1})	F_T ($\times$ 10^{-2}Nm^{-1})	F_O ($\times$ 10^{-2}Nm^{-1})
$x = 0.1$	527	410.28	2.024	1.227
$x = 0.2$	522	410.28	1.986	1.227
$x = 0.3$	526	410.28	2.017	1.227
$x = 0.4$	525	410.28	2.009	1.227
$x = 0.5$	527	410.28	2.024	1.227
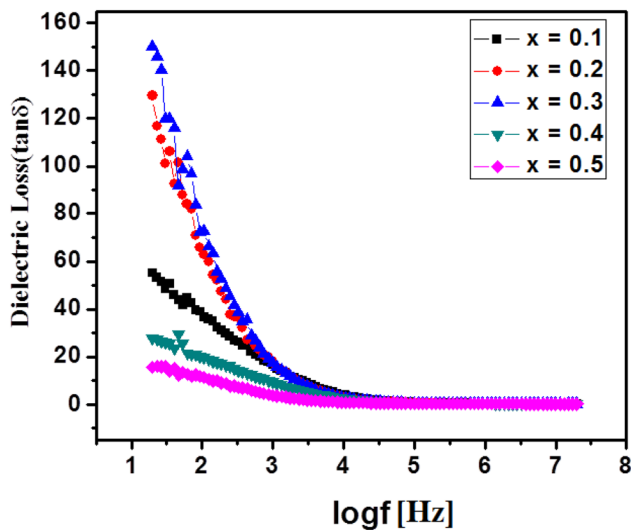
Fig. 6 Dielectric tangent loss vs log of frequency for Mn$_{1-x}$Cu$_x$Fe$_2$O$_4$ nanoparticles

saturated at higher frequencies. This variation is due to space charge polarization that arises from higher conductivity phase in the grain boundaries and localized due to gathering of charges due to applied electric field. The changing electric field will gather
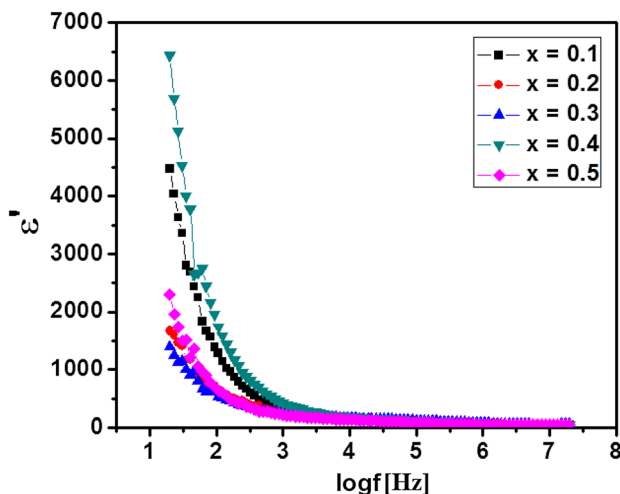
the charge carriers in the same axis, which takes finite time but at the particular frequency this phenomenon does not happen and this results in decrement of dielectric constant [39, 40].

Imaginary part of dielectric (complex dielectric constant) can be expressed as:

$$\varepsilon'' = \varepsilon_r \tan \delta, \tag{14}$$

where $''\varepsilon$ represents the imaginary part of relative dielectric constant and $tan\delta$ represents the dielectric or tangent loss. The imaginary part of relative dielectric constant (complex dielectric constant) deals with resistance of the ferrites. Frequency-dependent complex dielectric constant of copper-doped MFO as depicted in Fig. 8. It can be observed that complex dielectric constant (resistive behavior) of ferrites linearly decreases with increasing frequency and Cu^{2+} concentration. Space charge polarization affected this behavior and can be understood with assistance of Maxwell–Wagner Model [41] due to inhomogeneous morphological features.

The impedance loss and complex impedance of the ferrites express the contribution of grains and grain boundaries in the samples. The impedance loss (Z') of

Fig. 7 Relative dielectric constant vs frequency for Mn$_{1-x}$Cu$_x$Fe$_2$O$_4$ nanoparticles
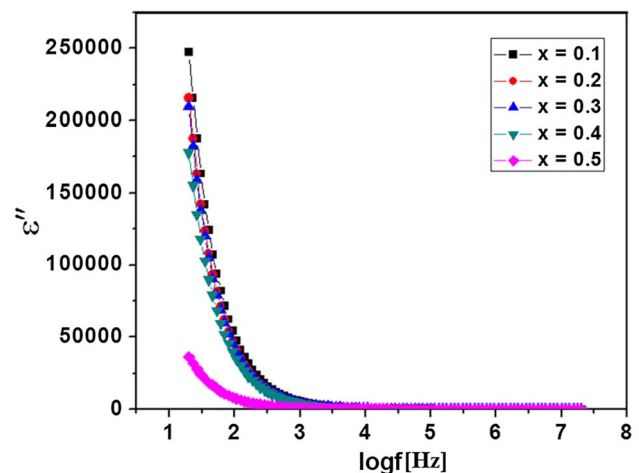
Fig. 8 Complex dielectric constant vs frequency for Mn$_{1-x}$Cu$_x$Fe$_2$O$_4$ nanoparticles

the $Mn_{1-x}Cu_xFe_2O_4$ nanoparticles is similar to the resistance applied in series as expressed below:

$$Z' = R_s \tag{15}$$

Figure 9 shows the variation in impedance loss with increasing frequency and revealed the conduction mechanism due to the hopping of electrons that is directly proportional to the frequency of applied electric field [42]. It has also been observed that the real part of impedance loss (Z′) increases with Cu^{2+} concentration. This behavior explained the space charge polarization in the samples. The merger of impedance loss at higher frequencies is due to the release of space charges.

The complex impedance loss can be determined by following equations:

$$Z'' = \frac{1}{2\pi f C_p}, \tag{16}$$

where Z″ is the complex impedance loss, f is the frequency of the applied electric field, and C_p is the parallel capacitance of the pellets.

The complex impedance loss of the ferrite samples as plotted in Fig. 10 shows revealed that the complex impedance loss (Z″) is arrived at the higher frequencies due to major contribution of the grains and grain boundary resistances. The observed peak corresponds to the dominating behavior of grain boundary resistivity over conductivity; however, the conductivity would be ignored at grain boundaries [43, 44].
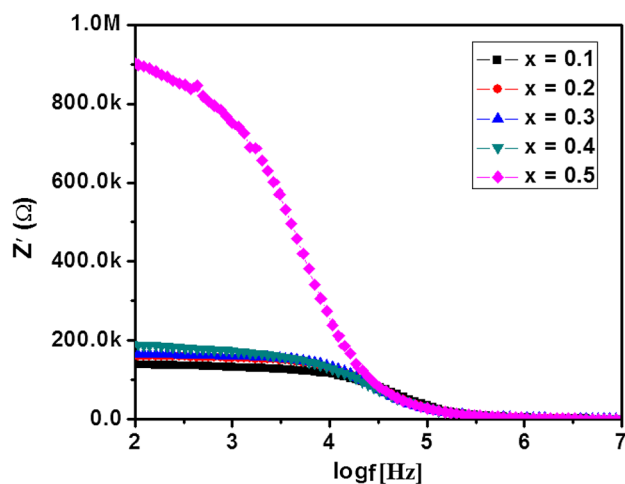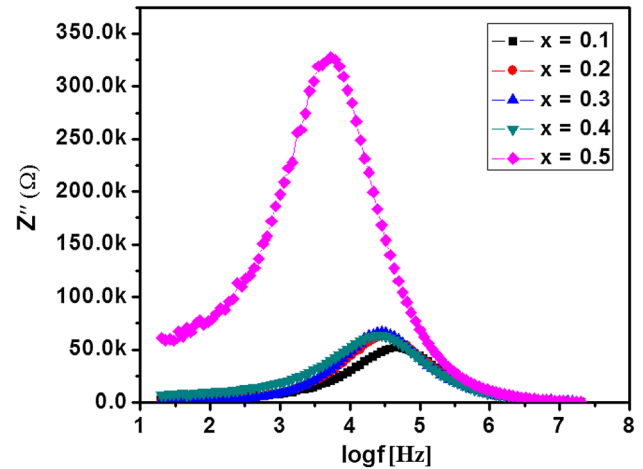
Fig. 10 Complex impedance loss vs frequency for $Mn_{1-x}Cu_xFe_2O_4$ nanoparticles

3.3.1 Nyquist plot

The electrical behavior of $Mn_{1-x}Cu_xFe_2O_4$ nanoparticles depends on contribution of grains and grain boundaries. The Nyquist plot (complex impedance and real impedance) has been drawn over wide range frequency and Cu^{2+} concentration to reveal the contribution of grains and grain boundaries as shown in Fig. 11. The existence of semicircle arc whose diameter increases with Cu^{2+} concentration is the result of contribution as DC conduction from grain boundaries [45]. This reinforces the idea of electrical mechanism that follows single relaxation characteristics [46]. The diameter of semicircles shows that the contribution of grain boundaries provides resistance in the sample, whereas capacitance depends over the estimation of maximum frequency of semicircle [47]. Cu^{2+} substitution increases the arc of semicircles and suggested a reduction in DC conductivity of ferrite nanoparticles. Therefore, resistive and capacitive characteristics of ferrites can be estimated through conduction and relaxation phenomenon associated with response of grain boundaries. Measured values of real (ε′) and imaginary (ε″) part of dielectric constant, tangent loss, real (z′) and imaginary (z″) part of impedance, real (M′) imaginary (M″) part of modulus and AC conductivity of $Cu_xMn_{1-x}Fe_2O_4$ nanoparticles are listed in Table 3.

3.3.2 Electric modulus

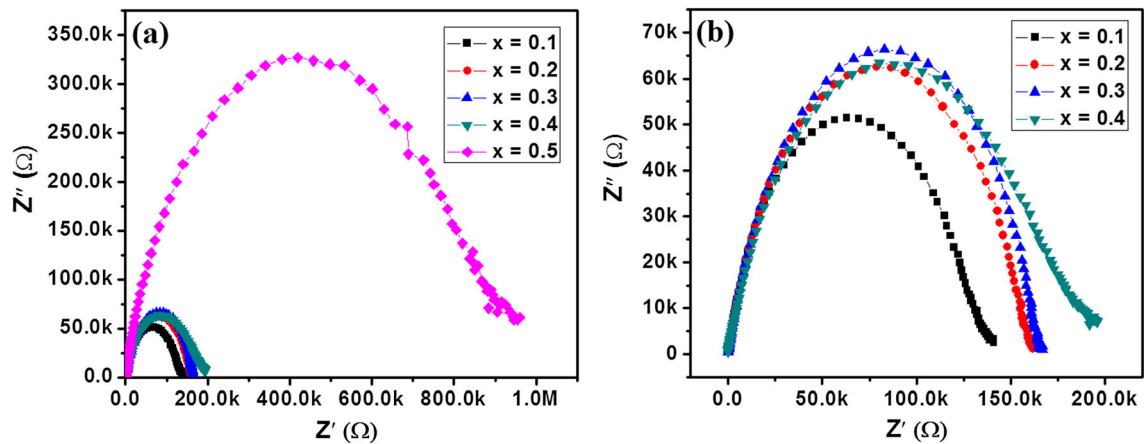The imaginary part of electric modulus (M″) can be calculated as [48]:

Fig. 9 Impedance loss vs frequency for $Mn_{1-x}Cu_xFe_2O_4$ nanoparticles

Fig. 11 Nyquist plots of $Cu_xMn_{1-x}Fe_2O_4$ spinel nanoparticles

$$M'' = 2\pi f C_p Z',\tag{17}$$

where M'' represents the imaginary part (complex) modulus, f is applied electric field frequency, Z' represents the real part of impedance loss, and C_p is the parallel capacitance of the pellets.

The complex electric modulus of the copper-substituted MFO ferrites in the range from 20 Hz to 20 MHz is plotted in Fig. 12. It can be observed that the real part of electric modulus of copper-substituted ($Mn_{1-x}Cu_xFe_2O_4$) nanoparticles increases exponentially toward lower frequencies for all samples. The real part of electric modulus varies also with copper substitution.

The real part of electric modulus (M′) was determined by using following expression:
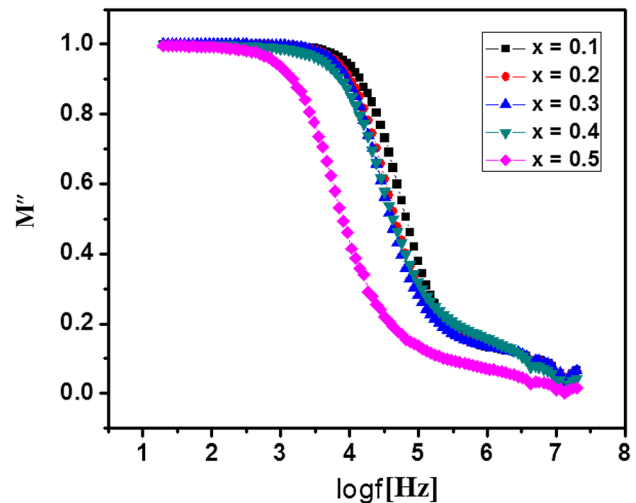

Fig. 12 Complex electric modulus vs frequency for $Mn_{1-x}Cu_xFe_2O_4$ nanoparticles

Table 3 Measured values of real (ε') and imaginary (ε'') part of dielectric constant, tangent loss, real (z') and imaginary (z'') part of impedance, real (M′) imaginary (M″) part of modulus and AC conductivity of $Cu_xMn_{1-x}Fe_2O_4$ ($x = 0.0$, 0.1, 0.2, 0.3 and 0.4)

Cu conc.	Frequency	ε'	ε''	Tan(δ)	Z′	Z″	M′	M″
$x = 0.1$	1 kHz	314.08	5271.24	16.78	133,000	7900	0.000011	0.00018
	50 kHz	109.83	134.10	1.221	62,900	51,500	0.00365	0.00446
	1 MHz	43.63	10.51	0.240	366	1520	0.02166	0.00521
$x = 0.2$	1 kHz	249.06	4482.90	17.99	156,000	8670	0.0000123	0.000222
	50 kHz	125.26	119.91	0.957	56,200	58,700	0.00416	0.00398
	1 MHz	46.45	11.26	0.242	346	1430	0.02033	0.00493
$x = 0.3$	1 kHz	245.86	4343.39	17.66	161,000	9110	0.0000129	0.000229
	50 kHz	134.59	117.41	0.872	51,900	59,500	0.00421	0.00368
	1 MHz	48.60	11.98	0.246	336	1360	0.01939	0.00478
$x = 0.4$	1 kHz	426.96	4007.79	9.38	173,000	18,400	0.0000268	0.000247
	50 kHz	133.48	124.07	0.929	52,700	56,600	0.00401	0.00373
	1 MHz	46.02	8.96	0.194	286	1470	0.02093	0.00474
$x = 0.5$	1 kHz	229.42	873.86	3.80	751,000	197,000	0.000281	0.00107
	50 kHz	100.37	46.82	0.466	53,800	15,000	0.00818	0.00381
	1 MHz	45.82	4.72	0.103	156	1510	0.02159	0.00222

$$M' = \frac{M''}{\tan \sigma}, \qquad (18)$$

where M' represents the real part of electric modulus, M'' represents the complex electric modulus, and $\tan\delta$ is the dielectric loss of pellet.

The real part of electric modulus shown in Fig. 13 revealed the variation in complex part of electric modulus of $(Mn_{1-x}Cu_xFe_2O_4)$ nanoparticles as a function of frequency up to 20 MHz due to contribution of insignificant electrode polarization, whereas conductivity relaxation process is obvious within the given frequency range. The conductivity relaxation shifted toward higher frequency range by the substitution of Cu^{2+} concentration. This behavior of the ferrites is non-Debye and occurred due to relaxation time distribution and the non-experimental approach of electrical functions. The maxima of the peak gives conductivity relaxation time with maxima because of the polarization mechanism [49].

3.3.3 Cole–Cole plot

The Cole–Cole plots for all the samples revealed that grains and grain boundaries are influenced by Cu^{2+} concentration as sharp semicircles are depicted in Fig. 14. In general, for the ferrite samples, two semicircles appear, one corresponds to grain and the other corresponds to grain boundaries. The existence of only one semicircle in the present case depicted that the contribution of grain boundaries is dominant and resulted in reduction of DC conductivity of ferrites.
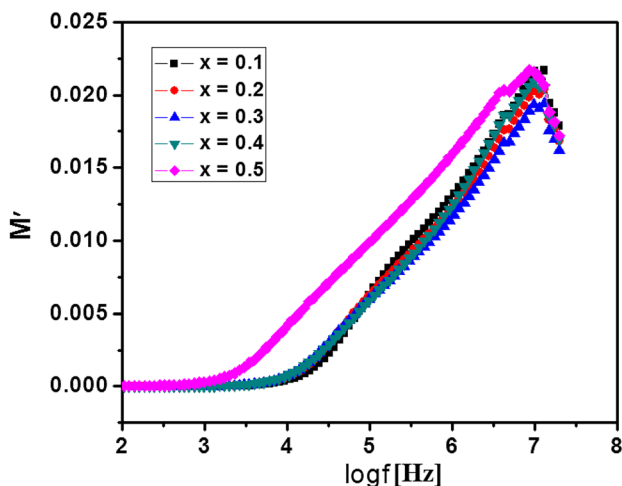

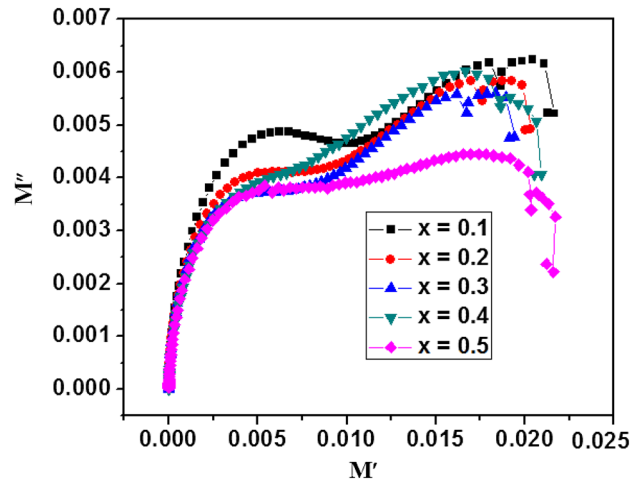**Fig. 13** Real part of electric modulus vs frequency for $Mn_{1-x}Cu_xFe_2O_4$ nanoparticles

Fig. 14 Cole–Cole (M' versus M'') plot for $Mn_{1-x}Cu_xFe_2O_4$ spinel ferrite nanoparticles

In these plots, semicircle is depicted only at low frequencies which means impedance characteristics of ferrites follows Cole–Cole formula [50]. It can be seen that semicircles shifted away from origin confirming the increment in resistance and relaxation characteristics of ferrite samples [51].

3.4 AC conductivity

The AC conductivity of the ferrite is determined as

$$\sigma_{ac} = 2\pi f \varepsilon_r \tan \delta, \qquad (19)$$

where σ_{ac} represents the ac conductivity, f represents the applied electric field frequency, ε_r is the dielectric constant of the medium, and $\tan\delta$ is the dielectric tangent loss of the medium. The dielectric tangent loss ($\tan\delta$), AC conductivity, and dielectric constant ($'\varepsilon$) were observed to decrease exponentially predicting the decrement in AC conductivity. Moreover, the higher dielectric dispersions observed at the low frequencies as plotted in Figs. 4, 5, and 6, respectively. The dielectric behavior of copper-substituted manganese ($Mn_{1-x}Cu_xFe_2O_4$) spinel ferrites can be explained by Maxwell–Wagner two-layer model with assistance of Koop's phenomenological theory [51].

The frequency of applied voltage and copper concentration in the ferrite samples can affect the conductivity. The frequency-dependent conductivity of $Mn_{1-x}Cu_xFe_2O_4$ nanoparticles as shown in Fig. 15 revealed that conduction reduces linearly as a function of copper concentration; however, it is observed to improve at lower frequency. The variation observed at higher frequencies is due to dipole
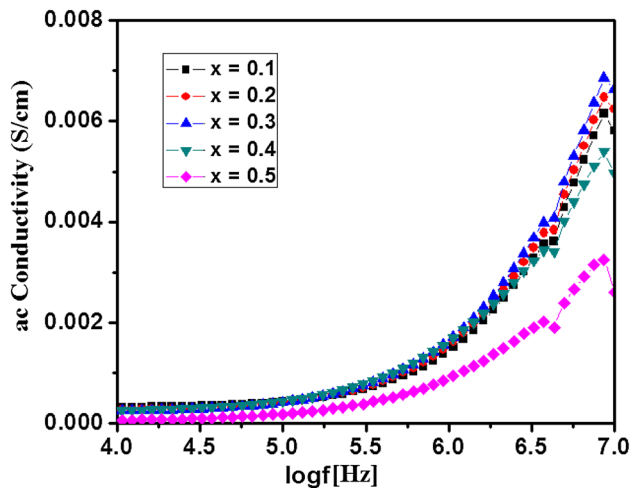
Fig. 15 AC conductivity vs frequency for $Mn_{1-x}Cu_xFe_2O_4$ nanoparticles

relaxation characteristics [52] of the samples validating their viability in sensors.

4 Conclusions

The copper-substituted manganese ($Mn_{1-x}Cu_xFe_2O_4$) spinel ferrite nanoparticles have been synthesized successfully *via* simple, eco-friendly, and effective sol–gel auto-combustion method. XRD analysis revealed that the $Mn_{1-x}Cu_xFe_2O_4$ exhibits cubic spinel structure with slight decrease in lattice constant as a function of Cu^{2+} substitution. The dielectric constant and dielectric loss observed to decrease as the frequency of applied electric field increases. These observations can be explained by space charge polarization in the light of Maxwell–Wagner two-layer model. The imaginary part of impedance, also called spectrum loss indicated only one semicircle, which shows the dominance of grains and the conduction through grain boundaries is negligible. The real part of impedance increases with Cu^{2+} concentration and frequency which suggested the reduction in conductivity of the samples. The prepared $Mn_{1-x}Cu_xFe_2O_4$ spinel ferrite nanoparticles with good capacitance might have potential to be used in microwave applications.

Acknowledgements

Compliance with ethical standards

Conflict of interest All the authors of this manuscript would like to declare that there is no conflict of interest regarding publication of this manuscript. Moreover, the authors have no known competing financial interests or personal relationships that could have appeared to influence the work reported in this paper.

References

1. J. Richardson, D. Yiagas, B. Turk, K. Forster, M. Twigg, Origin of superparamagnetism in nickel oxide. J. Appl. Phys. **70**(11), 6977–6982 (1991)

2. A.K. Zak, W. Abd Majid, M.E. Abrishami, R. Yousefi, Solid State Sci **13**(1), 251 (2011)

3. Wang ZL, Liu Y, Zhang Z, Handbook of Nanophase and Nanostructured Materials: Materials System and Application (I), Vol 3 (Kluwer Academic/Plenum Publishers, New York, 2003)

4. S. Mornet, S. Vasseur, F. Grasset, E. Duguet, Magnetic nanoparticle design for medical diagnosis and therapy. J. Mater. Chem. **14**(14), 2161–2175 (2004)

5. F.-Y. Cheng, C.-H. Su, Y.-S. Yang, C.-S. Yeh, C.-Y. Tsai, C.-L. Wu, M.-T. Wu, D.-B. Shieh, Characterization of aqueous dispersions of Fe3O4 nanoparticles and their biomedical applications. Biomaterials **26**(7), 729–738 (2005)

6. A.H. Lu, S. EeL, F. Schüth, Magnetic nanoparticles: synthesis, protection, functionalization, and application. Angewandte Chemie Int. Ed. **46**(8), 1222–1244 (2007)

7. C. Corot, P. Robert, J.-M. Idée, M. Port, Recent advances in iron oxide nanocrystal technology for medical imaging. Ad. Drug Deliv. Rev. **58**(14), 1471–1504 (2006)

8. A. Roca, R. Costo, A. Rebolledo, S. Veintemillas-Verdaguer, P. Tartaj, T. Gonzalez-Carreno, M. Morales, C. Serna, Progress in the preparation of magnetic nanoparticles for applications in biomedicine. J. Phys. D: Appl. Phys. **42**(22), 224002 (2009)

9. Schmid G, Nanoparticles: from theory to application (John Wiley & Sons, 2011)

10. Galasso FS, Structure and properties of inorganic solids: international series of monographs in solid state physics, vol 7 (Elsevier, 2016)

11. R.W. Wyckoff, *Crystall Structures: Miscellaneous Inorganic Compounds, Silicates, and Basic Structural Information*, vol. 4 (John Wiley and Sons Inc, New York, 1968).

12. B.K. Chatterjee, K. Bhattacharjee, A. Dey, C.K. Ghosh, K.K. Chattopadhyay, Influence of spherical assembly of copper ferrite nanoparticles on magnetic properties: orientation of magnetic easy axis. Dalton Trans. **43**(21), 7930–7944 (2014)

13. Viswanathan B, Murthy VRK, Ferrite materials: science and technology (Springer Verlag, 1990)

14. E. Şentürk, Y. Köseoğlu, T. Şaşmaz, F. Alan, M. Tan, RC circuit and conductivity properties of Mn0. 6Co0. 4Fe2O4 nanocomposite synthesized by hydrothermal method. J. Alloys Compd. **578**, 90–95 (2013)

15. Sekulić DL, Lazarević ZZ, Jovalekić ČD, Milutinović AN, Romčević NZ, Impedance spectroscopy of nanocrystalline MgFe2O4 and MnFe2O4 ferrite ceramics: effect of grain boundaries on the electrical properties. Sci. Sinter. **48**(1) (2016)

16. Z. Ullah, S. Atiq, S. Naseem, Influence of Pb doping on structural, electrical and magnetic properties of Sr-hexaferrites. J. Alloys Compd. **555**, 263–267 (2013)

17. H. Farooq, M.R. Ahmad, Y. Jamil, A. Hafeez, Z. Mahmood, T. Mahmood, Structural and dielectric properties of manganese ferrite nanoparticles. J. Basic Appl. Sci. **8**, 597–601 (2012)

18. R.R. Bhosale, R.V. Shende, J.A. Puszynski, Thermochemical water-splitting for H2 generation using sol-gel derived Mn-ferrite in a packed bed reactor. Int. J. Hydrog. Energy **37**(3), 2924–2934 (2012)

19. K.M. Batoo, Study of dielectric and impedance properties of Mn ferrites. Phys. B: Condens. Matter **406**(3), 382–387 (2011)

20. Z.Ž Lazarević, Č Jovalekić, A. Recnik, V.N. Ivanovski, M. Mitrić, M.J. Romčević, N. Paunović, B.Đ Cekić, N.Ž Romčević, Study of manganese ferrite powders prepared by a soft mechanochemical route. J. Alloys Compd. **509**(41), 9977–9985 (2011)

21. P. Guo, G. Zhang, J. Yu, H. Li, X. Zhao, Controlled synthesis, magnetic and photocatalytic properties of hollow spheres and colloidal nanocrystal clusters of manganese ferrite. Colloid. Surf. A: Physicochem. Eng. Asp. **395**, 168–174 (2012)

22. M. Ahmed, S. El-Dek, S. Mansour, N. Okasha, Modification of Mn nanoferrite physical properties by gamma, neutron, and laser irradiations. Solid State Sci. **13**(5), 1180–1186 (2011)

23. Y. Li, J. Jiang, J. Zhao, X-ray diffraction and Mössbauer studies of phase transformation in manganese ferrite prepared by combustion synthesis method. Mater. Chem. Phys. **87**(1), 91–95 (2004)

24. J. Bellini, S. De Medeiros, A. Ponzoni, F. Longen, M. De Melo, A. Paesano Jr., Manganese ferrite synthesized from Mn (II) acetate+ hematite freeze-dried powders. Mater. Chem. Phy. **105**(1), 92–98 (2007)

25. R. Misra, S. Gubbala, A. Kale, W. Egelhoff Jr., A comparison of the magnetic characteristics of nanocrystalline nickel, zinc, and manganese ferrites synthesized by reverse micelle technique. Mater. Sci. Eng.: B **111**(2–3), 164–174 (2004)

26. C.R. Vestal, Z.J. Zhang, Magnetic spinel ferrite nanoparticles from microemulsions. Int. J. Nanotechnol. **1**(1–2), 240–263 (2004)

27. J. Li, H. Yuan, G. Li, Y. Liu, J. Leng, Cation distribution dependence of magnetic properties of sol–gel prepared MnFe2O4 spinel ferrite nanoparticles. J. Magn. Magn. Mater. **322**(21), 3396–3400 (2010)

28. J. Hu, I.M. Lo, G. Chen, Fast removal and recovery of Cr (VI) using surface-modified jacobsite (MnFe2O4) nanoparticles. Langmuir **21**(24), 11173–11179 (2005)

29. A. Patterson, The Scherrer formula for X-ray particle size determination. Phys. Rev. **56**(10), 978 (1939)

30. M.H. Habibi, F. Fakhri, Low temperature preparation, characterization, magnetic measurements, thermal, optical, morphological and photo-catalytic properties of nano-size single phase nickel ferrite NiFe 2 O 4. J. Mater. Sci.: Mater. Electron. **28**(18), 13455–13463 (2017)

31. F.S. Tehrani, V. Daadmehr, A. Rezakhani, R.H. Akbarnejad, S. Gholipour, Structural, magnetic, and optical properties of zinc-and copper-substituted nickel ferrite nanocrystals. J. Supercond. Novel Magn. **25**(7), 2443–2455 (2012)

32. Kumar AM, Rao PA, Varma MC, Choudary G, Rao K, Cation distribution in Co 0.7 Me 0.3 Fe 2 O 4 (Me= Zn, Ni and Mn). J. Modern Phy. 2011 (2011)

33. Z. Wu, M. Okuya, S. Kaneko, Spray pyrolysis deposition of zinc ferrite films from metal nitrates solutions. Thin Solid Films **385**(1–2), 109–114 (2001)

34. A. Raut, R. Barkule, D. Shengule, K. Jadhav, Synthesis, structural investigation and magnetic properties of Zn2+ substituted cobalt ferrite nanoparticles prepared by the sol–gel auto-combustion technique. J. Magn. Magn. Mater. **358**, 87–92 (2014)

35. S. Assar, H. Abosheiasha, Effect of Ca substitution on some physical properties of nano-structured and bulk Ni-ferrite samples. J. Magn. Magn. Mater. **374**, 264–272 (2015)

36. H. Zaki, H. Dawoud, Far-infrared spectra for copper–zinc mixed ferrites. Phys. B: Condens. Matter **405**(21), 4476–4479 (2010)

37. K.A. Kumar, R. Bhowmik, Micro-structural characterization and magnetic study of Ni1. 5Fe1 .5O4 ferrite synthesized

through coprecipitation route at different pH values. Mater. Chem. Phys. **146**(1–2), 159–169 (2014)

38. A.A. Hossain, T. Biswas, T. Yanagida, H. Tanaka, H. Tabata, T. Kawai, Investigation of structural and magnetic properties of polycrystalline Ni0. 50Zn0. 50− xMgxFe2O4 spinel ferrites. Mater. Chem. Phys. **120**(2–3), 461–467 (2010)

39. M.J. Iqbal, M.N. Ashiq, I.H. Gul, Physical, electrical and dielectric properties of Ca-substituted strontium hexaferrite (SrFe12O19) nanoparticles synthesized by co-precipitation method. J. Magn. Magn. Mater. **322**(13), 1720–1726 (2010)

40. M.A. Rahman, A.A. Hossain, Electrical transport properties of Mn–Ni–Zn ferrite using complex impedance spectroscopy. Physica Scripta **89**(2), 025803 (2014)

41. K.W. Wagner, Zur theorie der unvollkommenen dielektrika. Annalen der Physik **345**(5), 817–855 (1913)

42. Kremer F, Schönhals A, Broadband dielectric spectroscopy. (Springer Science & Business Media, 2002)

43. R. Gimenes, Md. Baldissera, M. Da Silva, C. Da Silveira, D. Soares, L.A. Perazolli, M. Da Silva, M. Zaghete, Structural and magnetic characterization of MnxZn1− xFe2O4 (x= 0.2; 0.35; 0.65; 0.8; 1.0) ferrites obtained by the citrate precursor method. Ceram. Int. **38**(1), 741–746 (2012)

44. D.E. Gavrila, Dielectric spectroscopy, a modern method for microstructural characterization of materials. J. Mater. Sci. Eng. A **4**, 18–26 (2014)

45. M. Abdullah, A.N. Yusoff, Frequency dependence of the complex impedances and dielectric behaviour of some Mg-Zn ferrites. J. Mater. Sci. **32**(21), 5817–5823 (1997)

46. S. Khadhraoui, A. Triki, S. Hcini, S. Zemni, M. Oumezzine, Variable-range-hopping conduction and dielectric relaxation in Pr0. 6Sr0. 4Mn0. 6Ti0. 4O3±δ perovskite. J. Magn. Magn. Mater. **371**, 69–76 (2014)

47. B. Unal, Z. Durmus, A. Baykal, M. Toprak, H. Sozeri, A. Bozkurt, Synthesis, dielectric and magnetic characteristics of poly (1-vinyl-1, 2, 4-triazole)(PVTri)–barium hexaferrite composite. J. Alloys Compd. **509**(32), 8199–8206 (2011)

48. M.B. Hossen, A.A. Hossain, Complex impedance and electric modulus studies of magnetic ceramic Ni 02.7 Cu 0.10 Zn 0.63 Fe 2 O 4. J. Adv. Ceram. **4**(3), 217–225 (2015)

49. H.M. Chenari, A. Hassanzadeh, M. Golzan, H. Sedghi, M. Talebian, Frequency dependence of ultrahigh dielectric constant of novel synthesized SnO2 nanoparticles thick films. Curr. Appl. Phys. **11**(3), 409–413 (2011)

50. S. Li, W. Yang, M. Chen, J. Gao, J. Kang, Y. Qi, Preparation of PbO nanoparticles by microwave irradiation and their application to Pb (II)-selective electrode based on cellulose acetate. Mater. Chem. Phys. **90**(2–3), 262–269 (2005)

51. I. Gul, E. Pervaiz, Comparative study of NiFe2− xAlxO4 ferrite nanoparticles synthesized by chemical co-precipitation and sol–gel combustion techniques. Mater. Res. Bull. **47**(6), 1353–1361 (2012)

52. B.A. Hasan, Dielectric properties of vacuum evaporated SnS thin films. J. Nano Adv. Mater. **1**, 87–98 (2013)